17th AIAA/CEAS Aeroacoustics Conference (32nd AIAA Aeroacoustics Conference)
05 - 08 June 2011, Portland, Oregon

AIAA 2011-2937

Incorporating Actuation Effects in Reduced-Order Models for Feedback Control of Axisymmetric Jets

Aniruddha Sinha*, Andrea Serrani† and Mo Samimy‡
The Ohio State University, Columbus, OH, USA

Localized arc filament plasma actuators have demonstrated significant potential in controlling high-speed and high Reynolds number axisymmetric jets in open-loop. As a first step in incorporating feedback for this control system, we have recently developed an empirical reduced-order model of the essential flow dynamics in the unforced jet using Proper Orthogonal Decomposition and Galerkin Projection. This modeling protocol has been validated using an existing direct numerical simulation (DNS) database of a low Reynolds number Mach 0.9 jet developed by Freund.[1] The present article describes an extensive experimental effort undertaken on a high Reynolds number Mach 0.9 jet with two primary objectives. First, relevant unforced jet data is collected for deriving a reduced-order model of this high Reynolds number jet. The simulation of this model shows appreciable fidelity in the short term, which is sufficient for developing a feedback controller. Second, data for several salient forcing cases are collected to validate a proposed technique for incorporating actuation effects in the model. This latter objective is also guided by an implicit large eddy simulation (ILES) database of a forced high Reynolds number Mach 1.3 jet developed by Gaitonde.[2] The validation of the actuator model requires simulation over a long time, for which we resort to the reduced-order model developed earlier for the DNS database. The effect of actuation in this model is found to be remarkably similar to the effects observed in experiments as well as in the ILES data.

I. Introduction

This paper considers feedback-oriented reduced-order modeling of a forced, high-speed, and high Reynolds number axisymmetric jet. The objective of feedback control is mitigation of the turbulent mixing noise propagating to the far-field, *or*, enhancement of the bulk mixing to hasten dissipation. In either case, the large-scale structures in the shear-layer of the jet must be manipulated.[3,4] These structures arise naturally and randomly in unforced jets owing to inherent instabilities of the mean flow. The very same instabilities also make the flow highly receptive to perturbations at certain frequencies. Over the past several years, localized arc filament plasma actuators (LAFPAs) have been developed in the Gas Dynamics and Turbulence Lab (GDTL) at The Ohio State University. These actuators have demonstrated considerable control authority on the said large-scale structures in open-loop control experiments when deployed in an azimuthal array immediately upstream of the nozzle exit.[5–9] As in any control system, the performance of the LAFPAs in open-loop is a function of the jet operating conditions, which are subject to significant variations. Thus, a natural advancement towards practical implementation is to incorporate feedback control, which may guarantee robustness in the presence of such uncertainties.

In Ref. 10, a strategy was proposed for educing a reduced-order model (ROM) of an unforced jet. This model was validated using a direct numerical simulation (DNS) database of a Mach 0.9 low Reynolds number ($Re = 3600$, based on the jet exit diameter) jet developed by Freund.[1] The domain of interest for the objectives stated above is the vicinity of the end of the potential core (see Figure 1). The ROM is derived using the Galerkin procedure in two steps.[11] In the first step, the kinematics of the flow are assumed to reside on a low-dimensional manifold, so that the infinite dimensional flow variables are represented by an

*PhD Candidate, Dept. of Mechanical and Aerospace Engineering, AIAA Student Member.
†Associate Professor, Dept. of Electrical and Computer Engineering, AIAA Senior Member.
‡The Howard D. Winbigler Professor of Engineering, Dept. of Mechanical and Aerospace Engineering, AIAA Fellow, Corresponding author, samimy.1@osu.edu

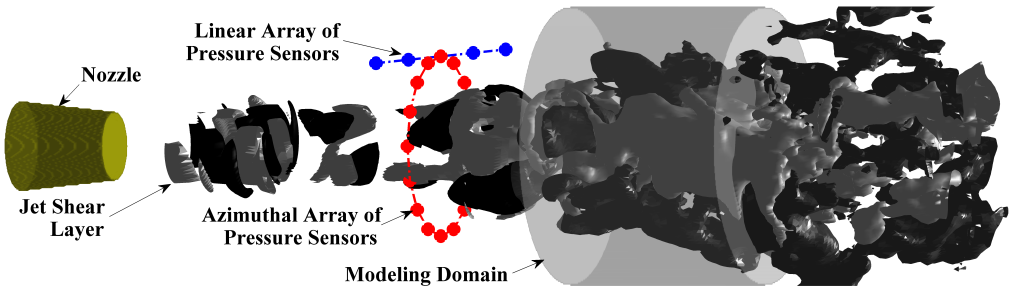

Figure 1. Schematic of the axisymmetric jet indicating the modeling domain and the model-state estimation strategy.

expansion on a finite number of basis functions. Proper Orthogonal Decomposition (POD) is the method of choice for educing such a basis. In the next step, the dynamics of these modes are also assumed to reside on the same low-dimensional manifold, and this is enforced by the Galerkin projection (GP) of the Navier-Stokes equations onto this manifold.

The goal of the present work is to incorporate the effect of control action exerted by plasma actuators in the jet model. The details of LAFPAs in the jet have not been fully replicated in numerical simulations, although significant fidelity has been achieved by Gaitonde[2,12] in implicit large eddy simulation (ILES) of a Mach 1.3 $Re = 1.1\times10^6$ jet under various forcing conditions. As such, the empirical data for the final reduced-order model must be derived from experiments, although intermediate validation is performed on DNS and ILES databases mentioned above. The experimental database required for incorporating compressibility effects in the model has to be built by simultaneously acquiring the velocity and two other thermodynamic quantities over a domain of feasible size. Till date, experimentalists have not realized this goal. These practical constraints impose the incompressibility assumption on the present ROM. The inaccuracies incurred by ignoring compressibility effects for the ROM under consideration have been shown to be within acceptable bounds.[10]

In the direct POD method,[13] the 2-point cross-correlation tensor needs to be known over the entire 3D domain of interest. This is quite unfeasible experimentally for any jet, particularly a high-speed and high Reynolds number jet. In the snapshot POD method,[14] one requires several snapshots of the three components of velocity over the 3D domain. This is also not directly achievable with present experimental techniques. However, Tinney et al.[15,16] showed that one can exploit the strong correlation between the velocity field and the pressure in the near irrotational field to reconstruct an approximation of such snapshots. They showed that the spectral variant of the well-known linear stochastic estimation, denoted SLSE, is appropriate for this purpose. The requisite spectral cross-correlation was obtained from time-resolved pressure measurements in a fixed configuration simultaneous with intermittent velocity measurements at known instants of the pressure record. Although the velocity must be measured with sufficient spatial density over the entire domain of interest for computation of the spatial derivatives, the measurements are not required to be simultaneous. To accelerate the data acquisition, 3-component particle imaging velocity (3C-PIV) was employed on several cross-stream slices of the jet. In the axisymmetric jet, the Fourier azimuthal domain of the velocity and pressure are both low-dimensional. This prompted the transformation of both measurements to the azimuthal modal domain and the retention of the lower modes only. Note that this necessitated the simultaneous measurement of pressure at multiple points distributed uniformly around the azimuth of the jet (see Figure 1). The 3C-PIV data on cross-stream slices was processed to obtain the lower order azimuthal modes of the velocity field. In addition, a 1D POD was performed on the azimuthal modal velocity field in the radial direction at each cross-stream slice to exploit its low-dimensionality. Finally, the spectral correlation was determined between the different azimuthal modes of pressure and all the lower order 1D POD modes of velocity in the corresponding azimuthal modes. The approximation of the above snapshots can be improved by employing an additional linear array of sensors, as shown in Figure 1.[10]

The next step in incorporating feedback control is to include the effect of forcing in the ROM of the unforced jet. To this end, an extensive experimental program was undertaken, as detailed in Section II. The modeling technique for the unforced jet was also validated using this experimental database of the high Reynolds number jet; the results are presented in Section III. A novel technique for incorporating the effect of LAFPA actuation in the model is described and validated in Section IV The research is summarized in Section V.

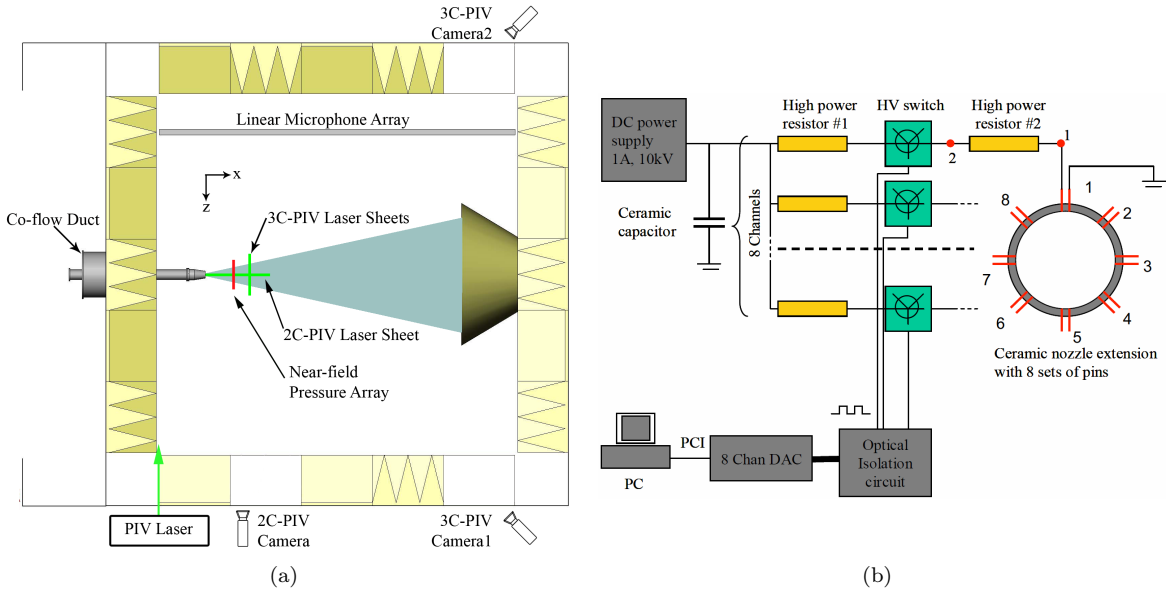

Figure 2. Schematic of (a) jet experimental facility at GDTL, and (b) LAFPA circuit.

II. Experimental setup

II.A. Flow facility

The jet at GDTL was created using compressed air discharging horizontally through a thick-lipped axisymmetric converging nozzle into an anechoic chamber before exhausting outdoors (see Figure 2(a)). The nozzle exit diameter was $D = 25.4$ mm and the Mach number was 0.9. The stagnation temperature typically stayed between 0 and 10°C depending on the operating conditions. The resulting variation in the exit velocity U_j was 277 m/s to 282 m/s, and the U_j during a particular run was used to normalize all the velocities measured during that run. The Reynolds number Re based on D and the exit conditions was $\sim 6.7 \times 10^5$.

II.B. Actuators

A brief description of the actuators follows; more information is available in previous publications from our lab.[5–7,9,17] Each LAFPA consists of a pair of 1 mm diameter tungsten pin electrodes connected to a high-voltage ($\sim$ kV) source through a dedicated high-frequency switching circuitry (see Figure 2(b)). A boron nitride nozzle extension with 25.4 mm inner diameter and $\sim$ 15 mm thickness was used to hold the actuators. Eight LAFPAs were distributed uniformly around the azimuth 1 mm upstream of the exit. A 0.5 mm deep and 1 mm wide ring groove is made in the extension to house the electrodes and shield the plasma. The center-to-center distance between the two electrodes in a LAFPA was 3 mm.

When the switch to a LAFPA is closed, the voltage across the electrodes ramps up to the breakdown voltage ($\sim$ 10 kV) in less than 10 μs. The air between the electrodes is ionized and an electric arc is established. Immediately afterwards, the voltage across the electrodes drops to a few hundred volts and remains at that level until the switch is opened. If all eight actuators are powered at the same time, the single actuator current is limited to 0.25 A. The computer-generated signal that manipulates the switching circuitry is a rectangular pulse train with independent control of frequency, duty cycle, and phase. The bandwidth of the actuators is 200 kHz, but the maximum forcing frequency used in the present work was $\sim$ 35 kHz. The relative phases of the eight actuators is controlled, and forcing can be achieved at simple azimuthal modes 0 to 3 and mixed modes 1, 2, and 4. Note that the amplitude of excitation cannot be controlled independently.

II.C. Data acquisition

A LaVision 3C-PIV system was used for 3-component velocity measurements on the cross-stream plane of the jet at discrete streamwise locations between $x/D = 5.0$ and 7.75 ($\Delta x/D = 0.25$). A Spectra Physics model

SP-400 dual head Nd:YAG laser was used as the light source. The two cameras used had 2048×2048 pixel CCDs, and the associated lenses resulted in a spatial resolution of about 0.096 mm on any cross-stream plane. The cameras were placed downstream of the jet exit outside the anechoic chamber obeying the Scheimpflug principle, with the line-of-sight access afforded by windows in the chamber (see Figure 2(a)). Vector maps were computed from image pairs separated in time by 1.4 μs. The cameras were kept fixed while the overhead optics were manipulated to place the laser sheet at various streamwise locations, a new calibration being performed for each PIV plane. The jet plume was seeded with diethylhexyl-sebecat liquid droplets atomized by a four-jet LaVision atomizer. A 381 mm diameter duct was placed co-axial with the jet to generate a very low speed ($\sim 0.01U_j$) entrained co-flow. The co-flow was seeded by a fogger to avoid statistical bias in the measurements, as well as spurious velocity vectors in the entrained air that has not mixed with the jet yet. The average droplet size was 0.7 and 0.25 μm for the jet flow and co-flow, respectively. For each experimental run, 1000 image pairs were recorded at about 2 Hz.

Three-component PIV processing consisted of a three-pass correlation routine with 64×64 pixel windows for the first pass and 32×32 pixel windows for an additional two passes, each pass having 50% overlap of windows. The resulting spatial resolution of the velocity map is $0.06D$. For the axisymmetric jet, it is natural to transform from rectangular to polar coordinates. The radial resolution was made $D/16$ and 80 grid points were placed around the azimuth. The radial domain was curtailed to $2D$. A triangle-based linear interpolation was used to transform the velocity map from the rectangular grid to the polar grid, before converting the velocity vectors to polar components.[15]

The pressure in the near irrotational field was measured using a combination of an azimuthal and a linear array (see Figure 1). The uniform azimuthal array had 16 sensors with their tips placed at $x/D = 3$ and $r/D = 1.5$. The linear array had 4 sensors at $x/D = 2.5$, 3.0, 3.5, and 4 on a meridional plane with their tips forming a line inclined at 8.6° to the jet axis; the second sensor was actually one of the azimuthal array sensors (see Figure 1). This configuration ensured that the sensors were approximately equidistant from the outer edge of the shear layer of the unforced jet, as measured in earlier PIV assays.[8] All 19 sensors were 1/4 in. B&K 4939 microphones attached to B&K 2670 pre-amplifiers. The microphone signals were band-pass filtered between 20 Hz and 100 kHz and amplified by B&K Nexus 2690 conditioning amplifiers before being *simultaneously* acquired using National Instruments A/D boards and LabView software. The frequency response of the microphones is flat up to 80 kHz with the microphone grid cover removed. Blocks of data were collected at 100 kHz with 4096 data points per block, resulting in 40.96 ms long records. Application of the discrete Fourier transform to this data gives a spectral resolution of 24.4 Hz.

For computation of pressure-velocity cross-spectral correlations, the timing of the 3C-PIV snapshots relative to the pressure measurements had to be carefully controlled. The LaVision PIV software was set up to generate a pulse signal 20 ms prior to the acquisition of each PIV snapshot. This pulse was used to trigger the acquisition of the corresponding block of pressure data. These timing characteristics ensured that each PIV snapshot was taken approximately in the middle of each pressure data block. However, instead of relying on this approximate relation, the Q-switch pulse that triggered the first laser was also acquired simultaneously with the pressure at the same sampling characteristics. In post-processing, the unique rising edge of this Q-switch pulse in each block of data was used to determine the location of the corresponding PIV snapshot in time.

For development of the empirical control-oriented reduced-order model of the jet, the behavior of the flow variables must be known relative to the forcing signal. In each experimental run with forcing, a unique forcing frequency and azimuthal mode was employed. The particular character of LAFPAs described above then means that the only unknown forcing information at any time is its phase. A sampling frequency of the order of MHz would have been required to educe the phase from the rectangular pulse train controlling the LAFPA operation. Instead, the pulse train controlling the first LAFPA was supplied to an Agilent 3320A 20 MHz arbitrary waveform generator, where each of square rising edges triggered a rising ramp signal. This sequence of ramp signals was acquired simultaneously with the pressure. Each ramp rose from 0 to 10 V within 20 μs, which is shorter than the smallest forcing time-period of interest, while being long enough to be sampled twice at the 100 kHz sampling rate. In post-processing of forcing cases, the ramp signal was decoded to determine the actuation phase at each pressure sample, and more importantly, corresponding to each PIV snapshot.

For additional validation, 2-component PIV was performed on a vertical meridional plane using much of the equipment and processing described above; the setup is depicted in Figure 2(a). This was *not* accomplished simultaneously with any other data acquisition. The resulting vector map had spatial resolution

of $0.093D$ and covered the entire jet plume over the axial domain between $0.3D$ and $12D$. For ensemble-averaged statistics, 1000 image pairs were recorded at about 5 Hz. In addition, sets of 250 images locked to various chosen phases of the actuation signal were also acquired for forced cases. Earlier attempts at locking PIV to LAFPA phases had failed at GDTL owing to high electromagnetic interference from the LAFPA power supply. In the current successful attempt, an intermediate pulse generator (Berkeley Nucleonics Corp. model 565) placed physically close to the LaVision computer was used to perform an additional thresholding of the noise-corrupted raw actuator control signal. The resulting cleaner signal was used to trigger the PIV capture.

III. Modeling Unforced Jet with Consideration of Forced Jet Data

The steps involved in educing an empirical ROM for the unforced jet have been detailed in Ref. 10, wherein the procedure was validated using a direct numerical simulation database of a Mach 0.9, $Re = 3600$ jet.[1] Many of these steps have been adopted from Refs. 15 and 16, wherein they were applied to a Mach 0.85, $Re = 1 \times 10^6$ experimental jet for a different purpose. The results at these common steps will not be detailed here. Instead, the discussion will focus on the novel application of these concepts to forced jet data.

The notation and non-dimensionalization are established first; the latter will be implicit in the ensuing presentation, unless otherwise mentioned. All linear dimensions and velocities are normalized by D and U_j, respectively. Pressure is normalized by $\rho_j U_j^2$, where ρ_j is the jet exit density. Time is normalized by the flow time scale D/U_j, and frequencies are normalized by its reciprocal. In particular, the forcing frequency f_F is represented by the non-dimensional forcing Strouhal number $St_{DF} = f_F D/U_j$, and the spectral frequency f is normalized to $St_D = fD/U_j$. The forcing azimuthal mode is denoted by m_F.

Employing cylindrical coordinates $\mathbf{x} := (x, r, \theta)^{\mathrm{T}}$, the modeling domain is $\Omega := [X_1, X_2] \times [0, R] \times \mathbb{T}$. Here, X_1 and X_2 denote the upstream and downstream bounds of the axial domain, R is the radial extent of the domain, and $\mathbb{T}$ is the circle group. The velocity vector is $\mathbf{U} : \Omega \times \mathbb{R} \rightarrow \mathbb{R}^3$, $\mathbf{U} : (\mathbf{x}, t) \mapsto (U_x, U_r, U_\theta)^{\mathrm{T}}$. The statistical stationarity and axisymmetry of the jet are used to define the mean velocity field as $\overline{\mathbf{U}}(x, r) := E\left\{(1/2\pi)\int_{-\pi}^{\pi} \mathbf{U}(x, r, \theta, t)\mathrm{d}\theta\right\}$. Henceforth, unless otherwise mentioned, the expectation operator $E(\cdot)$ will signify the ensemble-average. By symmetry $\overline{U}_\theta \approx 0$, and this is enforced explicitly in the implementation. The fluctuating velocity vector is defined as $\mathbf{u}(x, r, \theta, t) := \mathbf{U}(x, r, \theta, t) - \overline{\mathbf{U}}(x, r)$, with the three components being u_x, u_r, and u_θ, respectively.

The azimuthal direction is homogenous and periodic, so that any generic flow variable $w(\theta)$ lends itself to the azimuthal Fourier transform denoted by $w(\theta) \overset{\mathcal{F}_m}{\mapsto} \hat{w}(m)$; $\hat{w}(m) := (1/2\pi)\int_{-\pi}^{\pi} w(\theta)\mathrm{e}^{-\mathrm{i}m\theta}\mathrm{d}\theta$. Here m is the azimuthal mode. The inverse Fourier transform will be denoted by $\hat{w}(m) \overset{\mathcal{F}_\theta}{\mapsto} w(\theta)$; $w(\theta) = \sum_{m=-\infty}^{\infty} \hat{w}(m)\mathrm{e}^{\mathrm{i}m\theta}$. Accordingly, $\mathbf{u}$ is transformed as $\mathbf{u}(x, r, \theta, t) \overset{\mathcal{F}_m}{\mapsto} \hat{\mathbf{u}}(x, r, t; m)$.

The pressure at any point $\mathbf{x} = (x, r, \theta)^{\mathrm{T}}$ in the flow field at time t is denoted by $P(x, r, \theta, t)$. The time-average or ensemble average pressure is $\overline{P}(x, r) := E\left\{(1/2\pi)\int_{-\pi}^{\pi} P(x, r, \theta, t)\mathrm{d}\theta\right\}$. If information is not available at multiple azimuthal locations, as on the linear array depicted in Figure 1, then the azimuthal averaging is omitted. The fluctuating pressure is $p(x, r, \theta, t) := P(x, r, \theta, t) - \overline{P}^a(x, r)$. The azimuthal Fourier transform of p is defined in the usual manner (if information is available at multiple azimuthal locations): $p(x, r, \theta, t) \overset{\mathcal{F}_m}{\mapsto} \hat{p}(x, r, t; m)$.

In addition to experiments with the unforced jet, six different forcing cases were tested. In the axisymmetric $m_F = 0$ mode, the jet was forced at St_{DF} of 0.25, 0.30, and 0.35. These are near the jet column mode, where the most enhancement of bulk-mixing has been previously observed.[5,8] In the $m_F = 3$ mode, the jet was forced at St_{DF} of 1.5, 2.3, and 3.0. The largest reduction in far-field noise has been found to occur under these conditions.[6] Three-component PIV data was collected for the unforced jet on cross-stream slices located at $0.25D$ intervals between $5D$ and $7.75D$. For all the forcing cases, such data was acquired at the slices $x/D = \{5, 6, 7\}$. During all these measurements, the near-field pressure was acquired simultaneously in the configuration and procedure mentioned in Section II. The data from these forcing cases are analyzed below, and this analysis contributes to the model for the unforced jet.

Forcing the jet with $St_{DF} = 0.3$ and $m_F = 0$ has been known to generate well-defined axisymmetric structures.[5,8] In Figure 3, phase-averaged fields from the two different PIV experiments performed are compared. For the 3C-PIV experiments, phase-locking was not performed. However, the actuation phase was retrieved from the acquired data (see Section II), and a binning operation was performed to educe

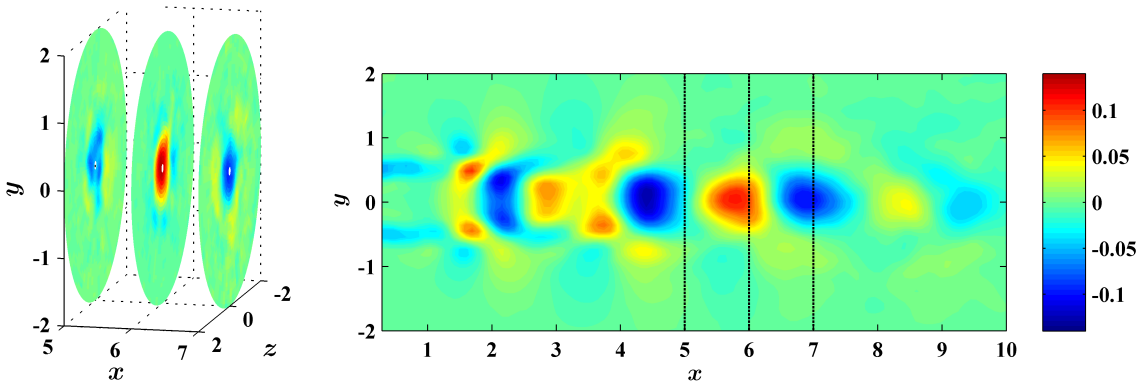

Figure 3. Comparison of u_x averaged at 45° phase of actuation with $St_{DF} = 0.3$ and $m_F = 0$ from (a) 3C-PIV on discrete cross-stream slices, and (b) planar PIV on meridional plane. The color scale is same for both sub-figures, and is normalized by U_j.

phase-averaged velocity fields for eight equally-spaced phases. The close match of the fields shown here lends credence to this phase-averaging procedure. Additionally, the fields agree closely with the results presented in Ref. 8, where a correlation-based conditional-averaging technique[18] was used to determine an approximately phase-averaged velocity field for the present forcing case. Under these forcing conditions, the length of the potential core was previously reported as $\sim 5D$.[8] The wavelength in the vicinity of the potential core end is observed to be $\sim 2.4D$ which, with the known St_{DF} of 0.3, gives a convective velocity of $0.72U_j$. This matches well with the value of convective velocity for axisymmetric structures reported for the *unforced* Mach 0.85 jet.[16]

In wall-bounded flows, boundary forcing or boundary movement may have a significant effect on the low-dimensional kinematic structure of the flow. In that case, empirical data from unforced and various forcing cases must be merged in order to educe a POD basis that spans all the different regimes of flow.[19–23] The question to be answered here is whether this is also the case for unbounded flows, in particular the free jet under consideration. For this purpose, the azimuthal and radial structure of the forced flows are analyzed vis-a-vis the unforced flow, as captured by 3C-PIV on the cross-stream sections.

Owing to the axisymmetry of the jet, it is natural to study the velocity field in its Fourier azimuthal domain, instead of the physical azimuthal domain. In Figure 4, the energies in the most pertinent azimuthal modes are shown. The energy in the mth azimuthal mode of the ith velocity component at the cross-stream slice location x is defined as

$$\varepsilon_i^{AZ}(x,m) := E\left\{\int_{r=0}^{R} |\hat{u}_i(x,r,t;m)|^2 r\mathrm{d}r\right\}. \tag{1}$$

The growth of total energy in this axial range, as well as the distribution of energies in the various azimuthal modes for the different components of velocity in the unforced jet, agree with previous results.[8,15,16,24–26]

It is observed in Figure 4 that when the forcing frequency is near the jet column mode (i.e. with $St_{DF} = 0.3$), all azimuthal modes are energized equitably even though the forcing azimuthal mode is axisymmetric. One consequence of the present discrete actuation method is that the excitation energy itself leaks into azimuthal modes other than the one intended. However, this effect has been determined to be relatively small. A more probable explanation is the nonlinear amplifying behavior of the jet which couples the energies between different azimuthal modes. Such nonlinearity is also captured by a quadratic interaction term in the reduced-order model described subsequently. For forcing at the much higher Strouhal number $St_{DF} = 3.0$ and $m_F = 3$, the modal energies are found to decrease at all azimuthal modes and at all measurement locations tested. This was expected from the reduction in the turbulent kinetic energy observed previously with these forcing parameters.[27] However, the novel result is that forcing does not significantly affect the *relative* azimuthal modal composition of the velocity field.

The next step is to investigate the low-dimensional structure of the flow in the radial direction. For this, a 1D scalar POD is performed separately for each azimuthal mode at each cross-stream slice where 3C-PIV

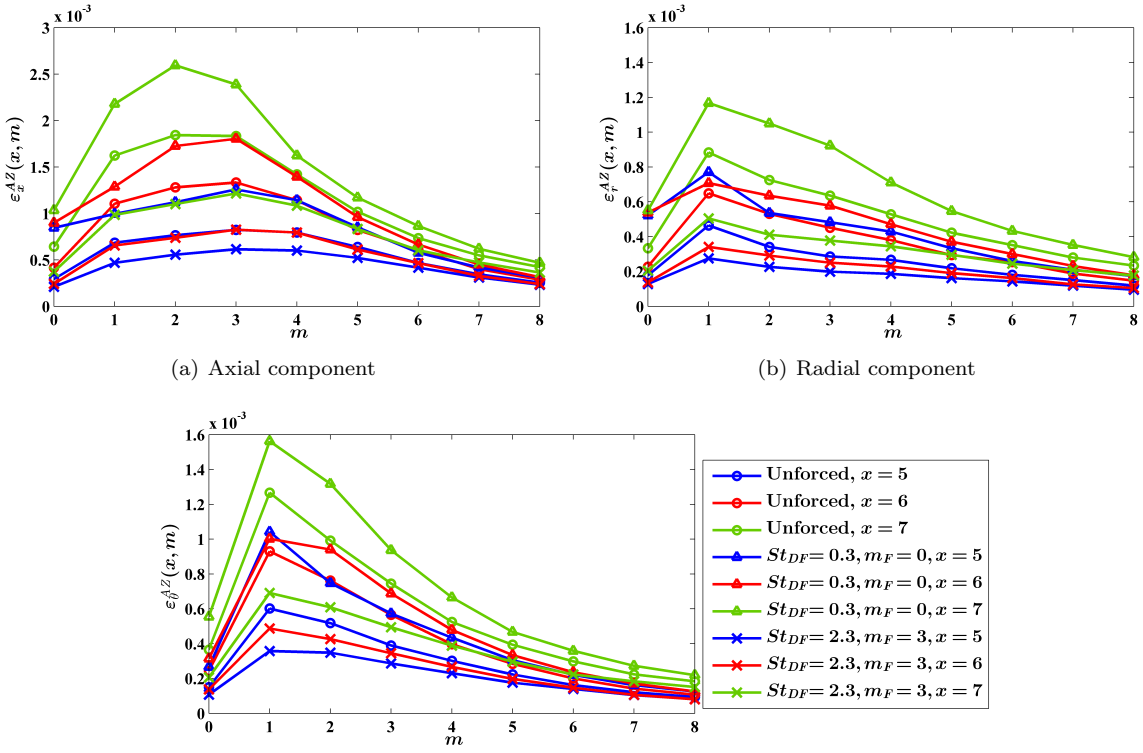

(a) Axial component

(b) Radial component

(c) Azimuthal component

Figure 4. Azimuthal modal composition of the three components of the velocity field. The forcing parameters and measurement locations are indicated in the legend. Note that the ordinate scales are disparate.

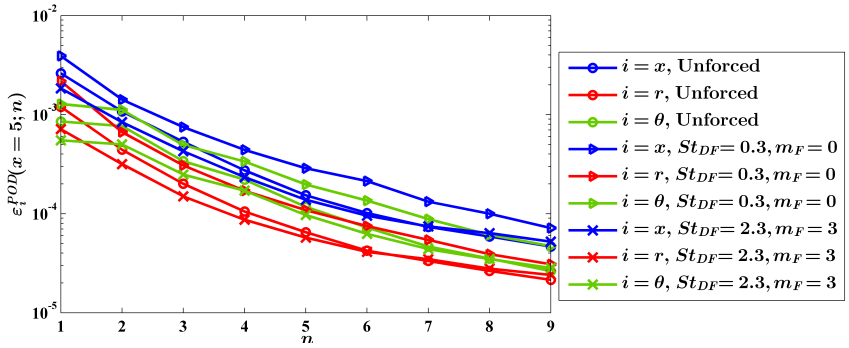

Figure 5. POD modal composition of the three components of the velocity field at $x = 5$ under different forcing conditions. The POD basis is derived from the unforced jet database, and for each mode, a summation is done over azimuthal modes 0 to 8.

data exist[8,10,15,16,24–26]

$$\hat{u}_i(x,r,t;m) \approx \sum_{n=1}^{N^1} \beta_i^{(n)}(x,m)\varphi_i^{(q)}(r;x,m). \tag{2}$$

Here φ and β are respectively the POD modal eigenfunction and corresponding modal coefficient, and N^1 is the number of 1D POD modes retained for azimuthal mode m. Exploiting the orthonormality of the POD basis, the energy captured in a POD reconstruction is defined as

$$\varepsilon_i^{POD}(x,n) := \sum_{m=-M^1}^{M^1} E\left\{\left|\beta_i^{(n)}(x,m)\right|^2\right\}, \tag{3}$$

where M^1 is the maximum azimuthal mode retained in the reconstruction. The POD basis may be computed

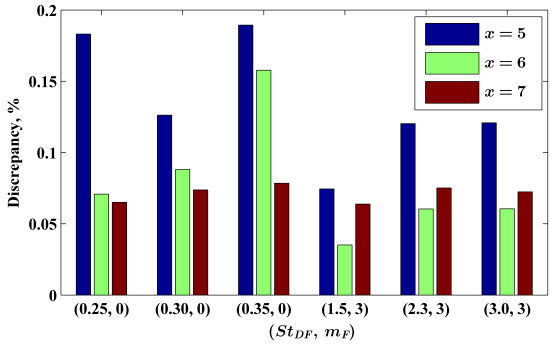

Figure 6. Changes in energy captured by a POD basis educed from a particular forced data vs. a basis obtained from the corresponding unforced data, expressed as a percentage of the total energy. All cases consider a 9-dimensional 1D scalar POD basis for azimuthal modes 0 through 8.

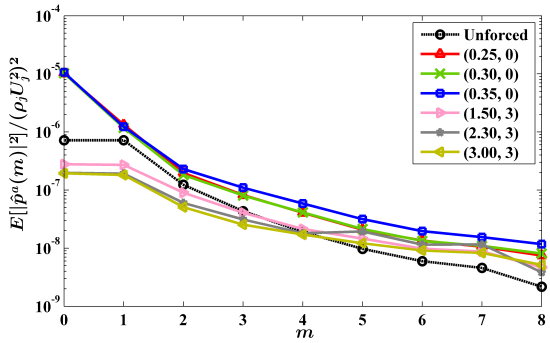

Figure 7. Effect of forcing on azimuthal modal composition of the near-field pressure at $x/D = 3$, $r/D = 1.5$. In the legend, the forcing cases are signified by (St_{DF}, m_F).

from the unforced jet database, and then used for projecting the velocity field for the different forcing cases. An alternate route is to compute the POD basis for reconstructing the velocity in a particular forcing case from the database of that case itself. Considering the first option, the resulting modal energies are compared in Figure 5, where x is set to 5 and $M^1 = 8$. It is observed that the POD modes are equitably energized or de-energized by forcing. To assess the difference in results obtained from the two options of constructing the POD basis, one needs to analyze the total energy captured at a particular x given by $\sum_{i\in\{x,r,\theta\}} \sum_{n=1}^{N^1} \varepsilon_i^{POD}(x,n)$. Figure 6 presents the discrepancy in this energy metric as a percentage of the total energy at x given by $E[1/2\pi \int_{\theta=-\pi}^{\pi} \int_{r=0}^{R} \{u(x,r,\theta,t)\}^2 r dr d\theta]$. One can readily conclude that the POD basis educed from the unforced flow is reasonable for a low-dimensional representation of the forced flows as well. This observation is crucial for justifying the later use of the ROM derived from the unforced jet database as the base for incorporating actuation effects.

Following Refs. 15 and 16, the time-resolved near-field pressure is employed here to estimate snapshots of the velocity field over an extended cylindrical domain. In Figure 7, the effect of forcing on the azimuthal modal composition of the near-field pressure is shown. Forcing in the axisymmetric mode with frequencies near the jet column mode is found to preferentially amplify the axisymmetric mode of pressure. Forcing in the third helical mode at much higher frequencies is seen to attenuate the azimuthal modes of pressure that were originally more energetic, resulting in a more equitable distribution of energy. This change in the azimuthal modal composition of the pressure is evidently different from the effect of forcing on the velocity field. This difference implies that the pressure-velocity correlations may be altered by forcing.

Before looking at the reconstruction of velocity fields under forcing, let us consider the unforced case. For the cross-stream slice at $x = 5.75$, 1976 snapshots were collected without forcing. This dataset was divided in two: one for modeling and the other for validation. Figure 8(a) presents the axial component of velocity fluctuations for a particular measured snapshot. The reconstruction from POD modes derived from the validation dataset itself is very faithful to the measured field (see Figure 8(b)). Spectral linear stochastic estimation (SLSE) coefficients were derived from the validation dataset, and the corresponding reconstruction shown in Figure 8(c) captures the shapes of the structures but under-predicts their amplitudes.

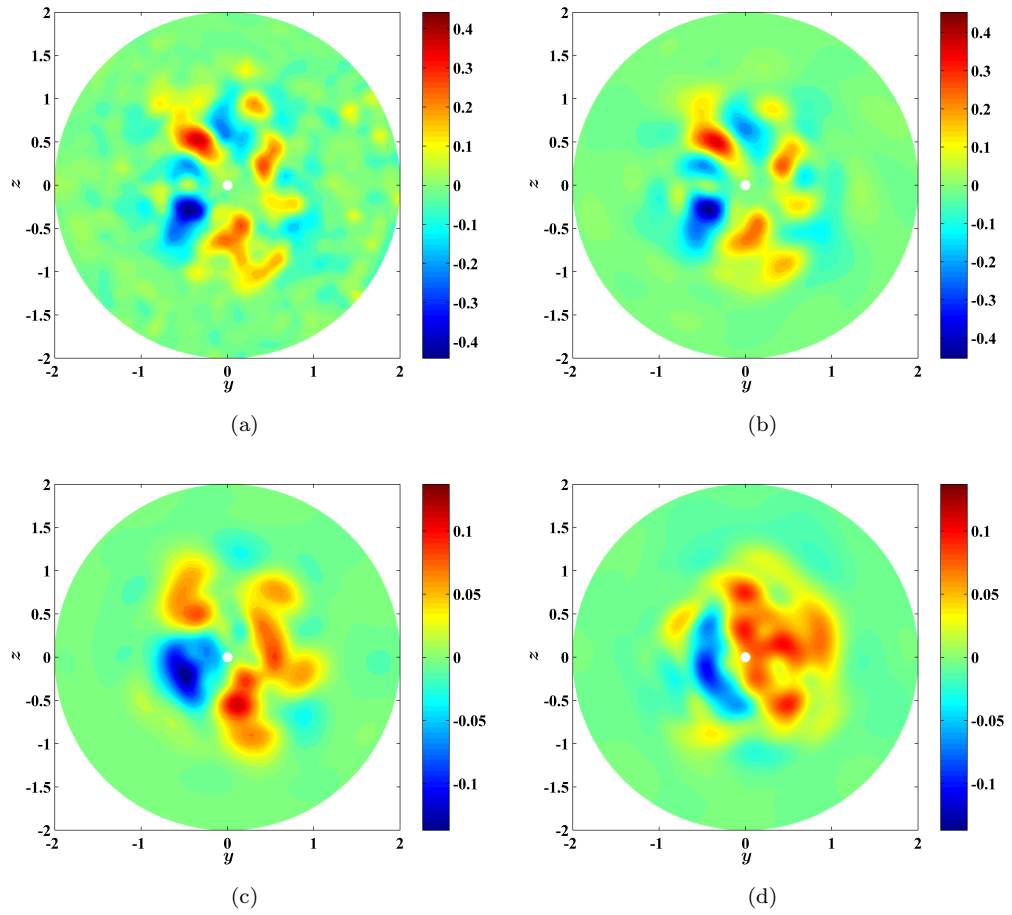

Figure 8. Snapshot taken from an unforced validation dataset of the axial velocity field at $x = 5.75$ obtained from (a) PIV, (b) reconstruction from POD modes derived from the validation dataset, (c) reconstruction from SLSE of the above POD modes, and (d) reconstruction from SLSE of POD modes derived from a separate modeling dataset. All reconstructions include azimuthal modes 0 through 8, and POD modes 1 through 9. Note the disparity in the color-scales representing u_x/U_j.

POD modes and their SLSE coefficients were also derived from the modeling dataset, and these were also used to estimate the same snapshot. The result is presented in Figure 8(d). Comparison of the last two sub-figures demonstrates the validity of this low-dimensional approximation approach.

The differences in the effect of forcing at $St_{DF} = 0.3$ and $m_F = 0$ on the velocity and pressure fields have been presented in Figures 4 and 7, respectively. Figure 9(a) presents the axial component of velocity fluctuations for a particular measured snapshot under these forcing conditions. Note that even with axisymmetric forcing, no axisymmetric structure can be distinguished herein. The SLSE coefficients were determined using the database of 1000 such snapshots with simultaneous pressure measurements. The reconstruction of the same snapshot using the associated pressure record and these estimation coefficients is presented in Figure 9(b). Owing to the strong axisymmetry of the pressure field (as noted in Figure 7), a strongly axisymmetric velocity field is erroneously estimated. The POD eigenfunctions educed from the unforced dataset have also been used to reconstruct the same snapshot in Figure 9(c). The appropriateness of this operation was remarked in the discussion regarding Figure 6, and can be observed here again. Finally, the SLSE coefficients educed from the unforced dataset have been used in conjunction with the pressure recorded simultaneous with the snapshot under consideration, and the resulting reconstruction is shown in Figure 9(d). Although the amplitudes of structures are under-predicted, their shapes are captured much better in comparison to Figure 9(b).

The foregoing discussion presented a qualitative assessment of SLSE. For a quantitative analysis, the

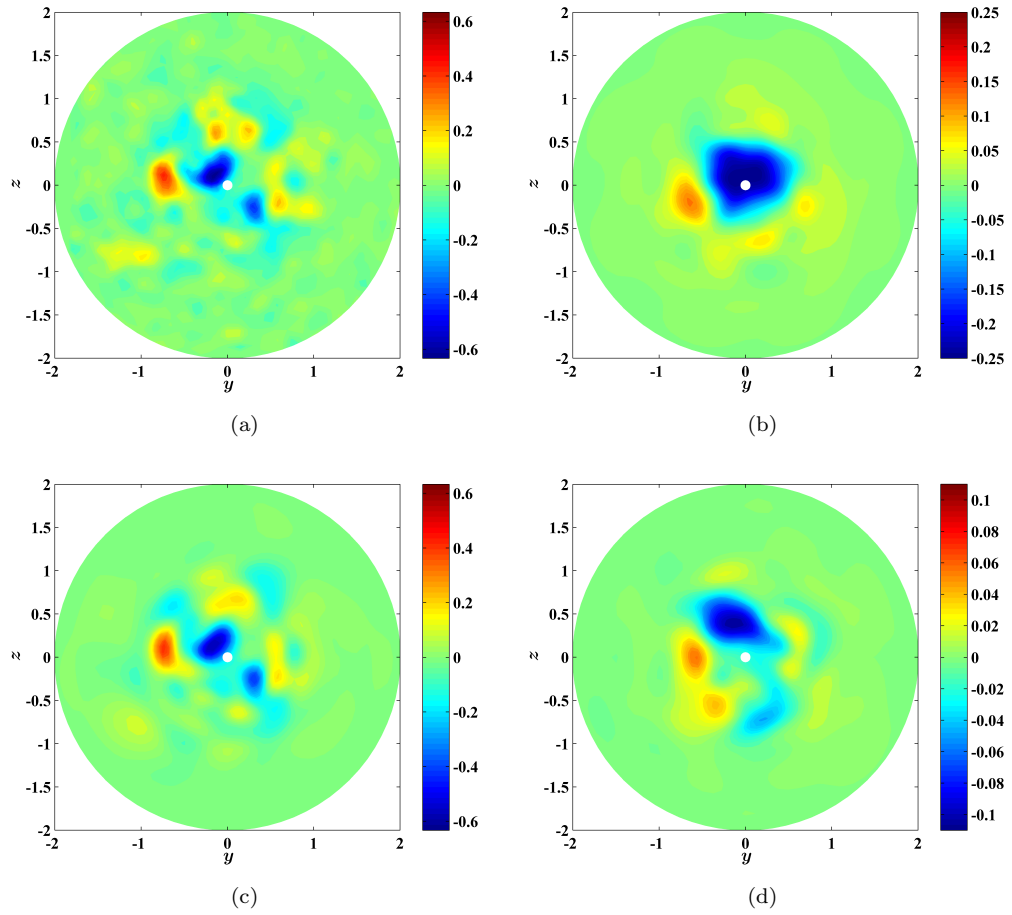

Figure 9. Snapshot of the axial velocity field at $x = 5$ with forcing at $St_{DF} = 0.3$ and $m_F = 0$, obtained from (a) PIV, (b) reconstruction from SLSE of POD modes derived from the same forced dataset, (c) reconstruction from POD modes derived from unforced dataset, and (d) reconstruction from SLSE of the above POD modes. All reconstructions include azimuthal modes 0 through 8, and POD modes 1 through 9. Note the disparity in the color-scales representing u_x/U_j.

following reconstruction error metric is defined

$$e_{recon} := \frac{E\left\{\sum_{i\in\{x,r,\theta\}}\sum_{x\in\mathcal{X}_v}\int_{-\pi}^{\pi}\int_{0}^{R}|\tilde{u}_i(x,r,\theta,t)-u_i(x,r,\theta,t)|^2 r\mathrm{d}r\mathrm{d}\theta\right\}}{\sum_{i\in\{x,r,\theta\}}\sum_{x\in\mathcal{X}_v}E\left\{\int_{-\pi}^{\pi}\int_{0}^{R}|u_i(x,r,\theta,t)|^2 r\mathrm{d}r\mathrm{d}\theta\right\}}, \tag{4}$$

where $\mathcal{X}_v$ refers to the set of x locations where PIV data are available. The approximation of any quantity such as w is denoted by $\tilde{w}$. Accordingly, $\tilde{u}$ refers to the velocity estimated by SLSE. The above metric is evaluated for a number of cases and the results are presented in Table 1. These were obtained with $\mathcal{X}_v = \{5, 6, 7\}$ and the first 9 POD modes were retained for each of the azimuthal modes from 0 to 8. Considering the first row of the table, the reconstruction errors are seen to be quite large. These should be contrasted to reconstruction errors of 0.73 and 0.56 obtained in the unforced DNS and ILES databases respectively with a similar setup of pressure sensing. Recalling that the ILES database simulated a jet with higher Reynolds number, the present result appears to be evidence of experimental uncertainty in computing the stochastic estimation coefficients. Considering the second row of the table, it is apparent that the SLSE coefficients educed from the unforced database is leading to greater errors in reconstructing the velocity fields in the forced cases. The discrepancy is less at the lower forcing frequencies near the jet column mode. In fact, it is negligible for the forcing case of $St_{DF} = 0.3$, $m_F = 0$ considered in Figure 9, reinforcing the conclusions drawn thereof. However, the discrepancy increases at the higher forcing frequencies. Previous

Database \ Forcing Case	Unforced	(0.25, 0)	(0.3, 0)	(0.35, 0)	(1.5, 3)	(2.3, 3)	(3.0, 3)
Self	0.9120	0.9341	0.9794	0.9650	0.9305	0.9299	0.9300
Unforced	0.9120	0.9878	0.9879	1.0029	1.0639	1.1371	1.1457

Table 1. The reconstruction error for SLSE applied to experimental data. The modeling database is either the same forcing case or the unforced case. The particular forcing case is denoted by the pair $(St_{DF},\ m_F)$.

research has established that forcing the jet with LAFPAs at these high forcing Strouhal numbers and higher helical modes results in smaller structures, and hence a higher-dimensionality of kinematics.[9,27,28] On the other hand, the near-field pressure signature filters out the effect of the smaller scales.[29] Such disparity in behavior of the pressure and velocity fields may explain the inaccuracies in reconstruction of the jet forced with higher forcing Strouhal numbers and $m_F = 3$ using SLSE coefficients derived from the unforced jet. In the remaining paper, the focus will remain on forcing cases around the jet column mode.

The foregoing developments results in a database of approximated three-component velocity fields over the 3D domain of interest. The low-dimensional representation of the above database involves Fourier decomposition in the azimuthal direction and 2D POD in the axial and radial directions.[10] The resulting expansion for the ith component of velocity is of the following form

$$u_i(x,r,\theta,t) \approx \sum_{m=-M}^{M} \sum_{n=1}^{N_m^2} \alpha^{(n)}(m)\Phi_i^{(n)}(x,r;m)\mathrm{e}^{\mathrm{i}m\theta}. \tag{5}$$

Here, Φ and α are respectively the POD eigenfunction and POD modal coefficient. The highest azimuthal mode retained is M and the number of POD modes retained for the mth azimuthal mode is N_m^2. The POD modes are derived from the unforced jet database, for reasons discussed above.

The subsequent Galerkin projection of the governing dynamics onto this POD basis results in a reduced-order model of the following form[10]

$$\begin{aligned}\dot{\alpha}^{(n)}(m) = \delta_{m,0}C_n + \sum_{n'=1}^{N_m^2} L_{nn'}(m)\alpha^{(n')}(m) + \sum_{m'=m-M}^{M} \sum_{n'=1}^{N_{m'}^2} \sum_{n''=1}^{N_{(m-m')}^2} Q_{nn'n''}(m,m')\alpha^{(n')}(m')\alpha^{(n'')}(m-m') \\ - \left| \int_0^R \hat{p}(x,r,t;m)\Phi_x^{(n)*}(x,r;m) r \mathrm{d}r \right|_{x=X_1}^{X_2}, \quad \forall m \in [0,M],\ \forall n \in [1,N_m^2].\end{aligned} \tag{6}$$

Here, C, L, and Q are respectively the constant, linear and quadratic coefficients of the ROM. They are derived from the POD basis and the base flow, which is the mean flow in this case. The last term requires knowledge of the pressure field over the inflow and outflow boundaries of the cylindrical domain. This information is not available for unforced jets, but modeling of this term in forced jets is the subject of the next section. For the unforced jet, this term was neglected in Ref. 10 following a similar omission in the case of a planar shear layer.[30,31] The term was evaluated in the DNS database that served as the testbench for this modeling effort in Ref. 10, and it was indeed found to be unimportant for the simulated dynamics.

The technique introduced in Ref. 10 for educing the ROM of the unforced jet has not been validated on high Reynolds number data previously. An ideal validation would consist of comparison of the velocity fields reconstructed from simulated trajectories with time-resolved and spatially-resolved measurements of the jet velocity field, but this is not possible. In lieu of this, such a field can be estimated from the time-resolved pressure field using SLSE. Basically, a moving window (in time) of pressure data is used to approximate the velocity field at the instant corresponding to the middle of each window. Several such snapshots are shown in Figure 10. An ROM was also created using the 15 most energetic modes from the experimental database. This was simulated in parallel, and the results are compared in Figure 10. The two fields are seen to be quite alike up to about 3.6 flow time steps. This is usually quite satisfactory for the purposes of developing a feedback controller.

The above comparison provides an intuitive understanding of the performance of the reduced-order model.

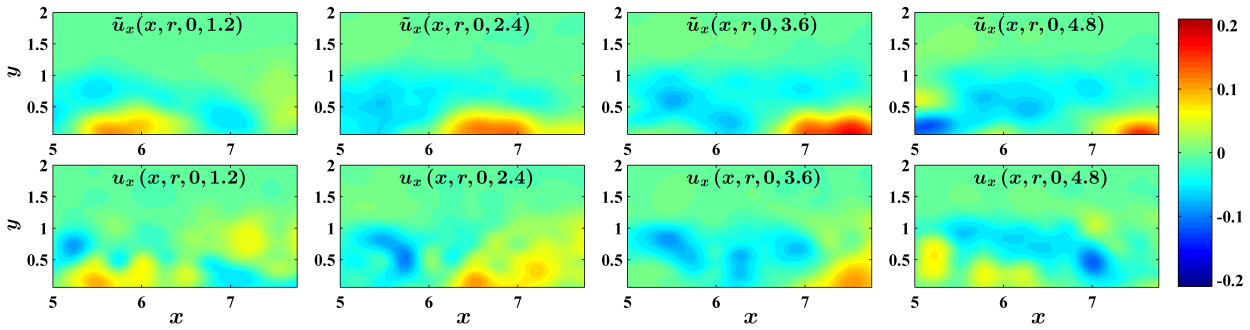

Figure 10. Axial component of velocity fluctuations on a meridional plane at various times measured from the start of simulation. The top row shows the simulated field and the bottom row shows the field estimated from pressure measurements. The common color-scale represents u_x/U_j.

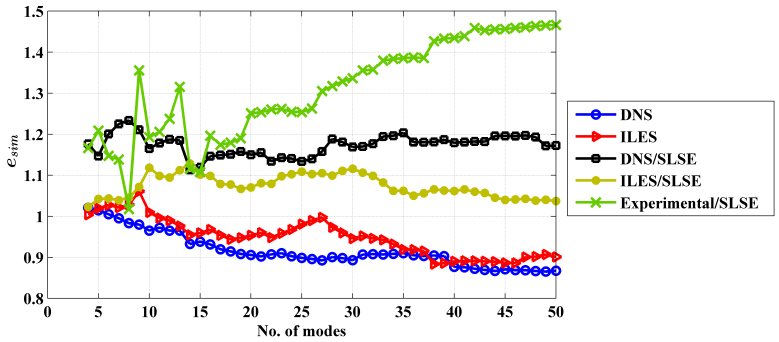

Figure 11. Simulation errors of reduced-order models of different dimensions derived from five different databases.

A more quantitative assessment is possible by examining the following metric of simulation error

$$e_{sim} := \frac{\sum_{i\in\{x,r,\theta\}} E\left\{\int_{-\pi}^{\pi}\int_{X_1}^{X_2}\int_0^R |\tilde{u}_i(x,r,\theta,t)-u_i(x,r,\theta,t)|^2 r\mathrm{d}r\mathrm{d}x\mathrm{d}\theta\right\}}{\sum_{i\in\{x,r,\theta\}} E\left\{\int_{-\pi}^{\pi}\int_{X_1}^{X_2}\int_0^R |u_i(x,r,\theta,t)|^2 r\mathrm{d}r\mathrm{d}x\mathrm{d}\theta\right\}}, \tag{7}$$

where $\tilde{\mathbf{u}}$ denotes the simulated velocity field. The expectation is evaluated over the simulation time horizon, which is 5 flow time steps. The error metric depends implicitly on the modeling parameters, and in particular the number of modes retained. It also changes somewhat with the chosen initial condition, so that a further averaging of the above ratio is performed by evaluating it with 20 different initial conditions for each of the data points reported below.

The simulation error metric is evaluated for ROMs derived from five different databases for the unforced jet. For each database, the 2D POD modes from all the azimuthal modes were sorted in descending order of their energies. Then, a ROM retaining a particular number of modes actually retained the most energetic modes from the above sorting. Models were derived from the DNS and ILES databases directly, and the corresponding simulation errors are shown in Figure 11. Both cases have a slight decreasing trend of errors with increasing number of modes retained. More remarkably, the simulation errors are very similar for ROMs obtained from these databases despite their large disparity in Reynolds number as well as Mach number. This leads to the conclusion that the essential dynamics of the coherent structures that are modeled herein are quite similar in these two cases. Note that the modeling of the DNS database was reported in Ref. 10.

It has been discussed previously that for experimental databases, one has to take recourse in SLSE to arrive at the low-dimensional model. To assess how this affects the simulation errors, SLSE was performed on the DNS and ILES databases, and the resulting estimated databases were then used to build ROMs. Figure 11 shows the performances of these models. It is evident that the route of SLSE introduces further errors in the models. The models from the ILES databases consistently out-perform those from the DNS

database in this case. This is surprising since the Reynolds number for the ILES database is much higher than that of the DNS database, so that one might have expected more modes to have been required to model the greater variety of scales. This result bears further analysis.

Finally we focus on the performance of the ROMs derived from the experimental database (using SLSE). The simulation errors are depicted in Figure 11. Neglecting the aberrant case of the 8-mode model, one observes that a 15-mode model has the greatest fidelity. This explains the detailed consideration of the simulation results from this model in the discussion surrounding Figure 10. One also notes that simulation errors increase with increasing number of modes, which is an inversion of the trend observed for the other cases in Figure 11. This may be a result of the large reconstruction errors observed with SLSE for the experimental database (see Table 1). However, the simulation error metric for the 15-mode model of the experimental database is seen to be very similar to the errors obtained with 15-mode models of the DNS and ILES databases through the SLSE route.

It must be mentioned here that, although the short-time behavior of the models from the experimental and ILES databases are satisfactory, the simulated trajectories actually became unbounded within about 40 flow time scales. On the other hand, the trajectories of the ROM derived from the DNS database remained bounded for at least an order of magnitude longer. The reason for this difference is the disparity in the Reynolds number. Although artificial diffusion is added to the ROM using an energy conservation algorithm,[10,32] it was still insufficient to guarantee long-term boundedness for the high Reynolds number flow. Feedback controllers need very low-dimensional models to be computationally tractable in real-time, so that incorporation of more modes is rarely feasible. Thus the above model represents a trade-off between fidelity and usability.

IV. Modeling actuation effects

In the free jet under consideration, the modeling domain chosen is downstream of the actuator location (see Figure 1). So the actuation term cannot be prescribed directly. The effect of actuation is modulated by the intervening axial length of the mixing layer of the jet before reaching the model domain through convection. Careful inspection of the proposed model in eqn (6) reveals that the only entry point of actuation effects is the pressure term. This means that the pressure field needs to be known at all times at the inflow and outflow boundaries of the modeled domain. Such information is not readily available from experiments. However, from experiments, one has knowledge of the fluctuating velocity field over forcing cycles. To utilize this information in determining the pressure field, the vortex model proposed by Lau et al.[33,34] will be invoked in the following development.

IV.A. Vortex model of Lau et al.

Lau et al.[33] proposed a very simple, elegant and intuitive relation between the pressure and velocity fields in the jet. Figure 12 is adapted from Ref. 33 and explains the original vortex model succinctly; a brief description follows. The mixing layer of the jet is supposed to consist of large-scale coherent structures convecting downstream. The original vortex model addressed the core and entrainment regions only (see Figure 12). Consider an observer at station (1) relative to the vortex street. The radial velocity fluctuations are positive in both the core and entrainment regions whereas the pressure and axial velocity fluctuations should vanish. Thus, the latter quantities are in quadrature with the radial velocity. When the observer is at station (2), the radial component should vanish at both the core and entrainment regions, whereas the pressure fluctuations should reach their most negative values in both regions. The axial velocity fluctuations would be positive in the core and negative in the entrainment region. Thus in both regions, pressure and axial velocity fluctuations are out-of-phase, and pressure fluctuation is in quadrature with and leads the radial velocity fluctuation. The axial and radial velocity fluctuations are in quadrature in both regions, with the former lagging the latter in the core and leading in the entrainment region.

Lau et al.[33] noted that closer inspection of this simple model reveals that there should be no Reynolds stresses in the mixing region, contrary to experimental findings. Later they proposed a refinement of the earlier model to address this issue,[34] wherein viscosity was implicitly invoked to argue for a non-linear interaction that leads to a positive Reynolds stress in the mixing layer.

The validating experimental results presented in Ref. 33 were obtained with a 2 inch nozzle run at Reynolds numbers between 1×10^5 and 3×10^5 (speeds ranged from 31 to 92 m/s). The first question to

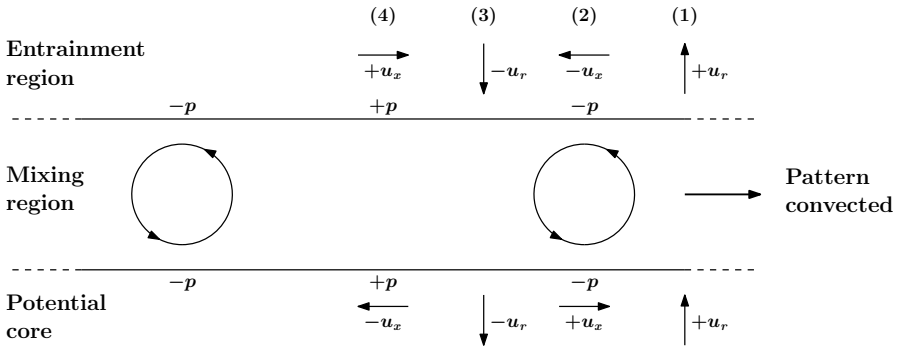

Figure 12. Vortex model of pressure-velocity relationship in a jet adapted from Ref. 33.

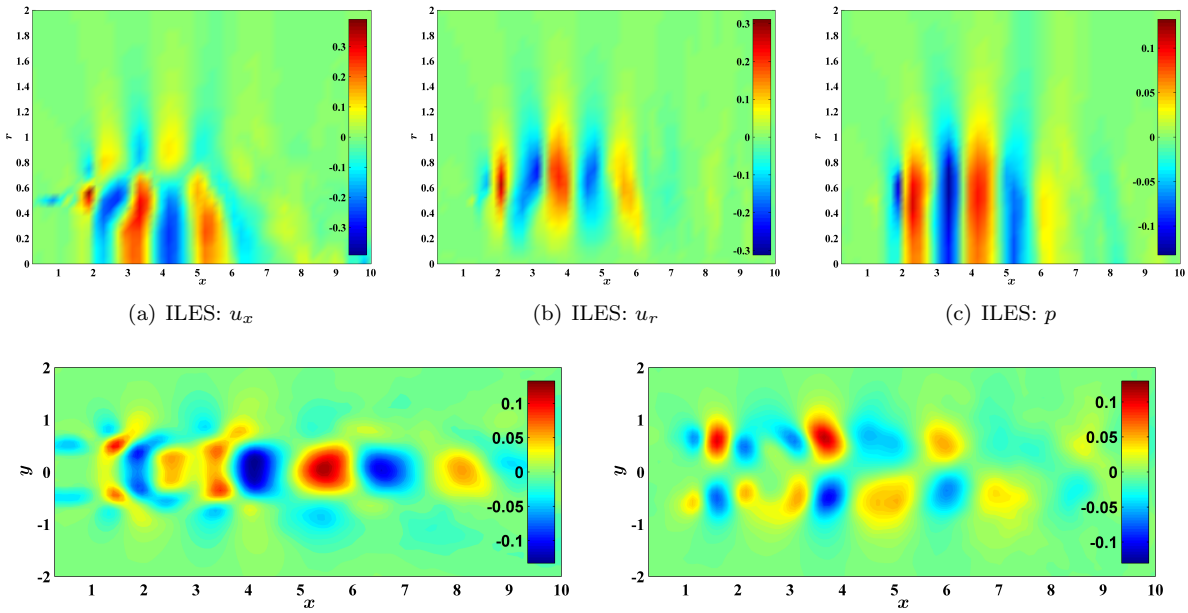

(a) ILES: u_x (b) ILES: u_r (c) ILES: p

(d) Experiment: u_x (e) Experiment: u_y

Figure 13. Phase-averaged contours of pressure and velocity fluctuations from two databases for $m_F = 0$ and $St_{DF} = 0.3$.

be answered here is whether this simple model can be useful at higher speeds. To this end, the temporal correlations of pressure and velocity are investigated for the ILES at database of the forced jet (Mach 1.3 and $Re = 1.1 \times 10^6$). The end goal is to extend the results to an experimental database of Mach 0.9 and $Re = 0.67 \times 10^6$ for which only velocity data exists.

To focus attention on the relevant statistics, it is pertinent to first discuss the similarity of the ILES results with open-loop experiments. Forcing the jet in the axisymmetric mode with frequency near the column mode has been found to produce very robust and repeatable structures. Figure 13 shows results with $m_F = 0$ and $St_{DF} = 0.3$ from both the ILES database and experiments. Figures 13(a)–13(c) present phase-locked velocity and pressure fluctuations from the ILES database for this forcing case. These are obtained by choosing any one snapshot and then all other snapshots that are an integer number of forcing periods away from it on the time axis, there being 6 such forcing periods in the saved database. The axisymmetric mode of forcing is exploited to perform a further averaging over the azimuth. The resulting average minus the average of the entire ensemble gives the phase-averaged fluctuations. On the other hand, Figures 13(d) and 13(e) shows the phase-averaged velocity fluctuations computed in post-processing of the phase-locked 2C-PIV experiments described in Section II. Note that the $y-$component of the velocity is measured by PIV, and it coincides with the radial velocity for the top half and the negative of the radial velocity over the bottom half of Figure 13(e).

In discussing the above forcing results, the first focus is on the axial velocity fluctuations from the ILES

and experimental databases in Figures 13(a) and 13(d). Several remarks are in order: (*a*) The amplitude of the fluctuations in the ILES database are about thrice those obtained from experiments. Recall that these are normalized by the jet exit velocity. (*b*) The shapes of the structures are similar over the axial domain up to $x \approx 5.5$. The similarities include the extents, geometries, and relative strengths of the structures. The induced velocity field is also seen to affect the potential core similarly. (*c*) Further downstream, there is a very quick drop in the strength of the structures from the ILES database. However, the experimental database shows large and strong structures spanning the jet centerline up to $x \approx 8.5$. Such a discrepancy in the potential core length between experiment and LES prediction has been reported before[35] and it has been found to be $\sim 2D$ for the present ILES database.

The remarks made for the axial velocity fluctuations hold for the radial velocity fluctuations in the most part (see Figures 13(b) and 13(e)). There is a similar discrepancy in the amplitude of the fluctuations. The upstream structures display similarities, but there are some discrepancies in the structures spacing and relative shapes and sizes. However, the characteristics at $x = 5$ are rather similar. Moreover, the drop off in structure strength further downstream is similar in the two databases for the radial component of velocity.

The phase-locked pressure fluctuations from the ILES database are presented in Figure 13(c). Recall that for the purpose of ROM development, the interest is in the radial distribution of pressure at $x = 5$ and $x = 8$, the inflow and outflow boundaries of the domain spanning the end of the potential core. Pressure fluctuations are negligible at the outflow boundary. This is of immediate practical importance since one can safely ignore the anomalies in the correlations in the ILES database that appeared at downstream stations, as discussed above. At the inflow boundary, the pressure fluctuations are strong, and appear as homogenous wavefronts covering the radial domain from the centerline to about one jet diameter. Further out radially, the wavefronts still appear flat, but the amplitude is diminished. This is the behavior that one wants to replicate for an approximate pressure field for the experimental database. The foregoing discussion serves as the background for the following considerations of the correlations pertaining to the vortex model.

The tool to study the pressure-velocity relationship is the single-point normalized temporal cross-correlation. The single-point temporal cross-correlation between the fluctuations of any two flow variables α and β is defined as

$$\Pi_{\alpha\beta}(x, r, t') := E\left\{\frac{1}{2\pi}\int_{-\pi}^{\pi} \alpha(x, r, \theta, t + t')\beta(x, r, \theta, t)\mathrm{d}\theta\right\}, \tag{8}$$

wherein the axisymmetry and stationarity of the jet are implicitly invoked. The corresponding normalized quantity is

$$R_{\alpha\beta}(x, r, t') := \frac{\Pi_{\alpha\beta}(x, r, t')}{\{\Pi_{\alpha\alpha}(x, r, 0)\Pi_{\beta\beta}(x, r, 0)\}^{1/2}}. \tag{9}$$

For proper comparison of results, the radial coordinate must be converted to the radial similarity variable (see Ref. 36 and references therein):

$$\eta(x, r) := \frac{r - r_{1/2}(x)}{\delta_\theta(x)}, \tag{10}$$

where $r_{1/2}$ is the jet half-width at half-maximum mean axial velocity $\overline{U}_x(x, r = 0)$ and δ_θ is the shear layer momentum thickness, both evaluated at a particular axial station x. Additionally, the time separation variable, t', will be normalized by the local flow time scale to obtain

$$\tau(x) := \frac{t'\overline{U}_x(x, r = 0)}{\delta_\theta(x)}. \tag{11}$$

Figure 14 shows the temporal velocity-pressure correlations at $x = 5$ in the ILES database for the case of forcing with $m_F = 0$ and $St_{DF} = 0.3$. Although the vortex model of Lau et al.[33,34] was validated for an unforced jet, the results presented here show that the model can explain the behavior of this forced high Reynolds number jet remarkably well. The predicted phase relations as well as the radial variations of the correlations follow the vortex model closely. The periodicity of the correlations are the result of the creation of robust repetitive structures due to the forcing. Figure 13 indicated that at this axial station coherent fluctuations span the potential core, and the core-type behavior is seen in the correlations here over a significant radial extent too. This is signaled by the anti-correlation of axial velocity with pressure, as explained in Figure 12. Schlieren images in experiments of this forcing case have confirmed the existence of such strong ring-like structures in the mixing layer that induce corresponding coherence in the potential core.[37]

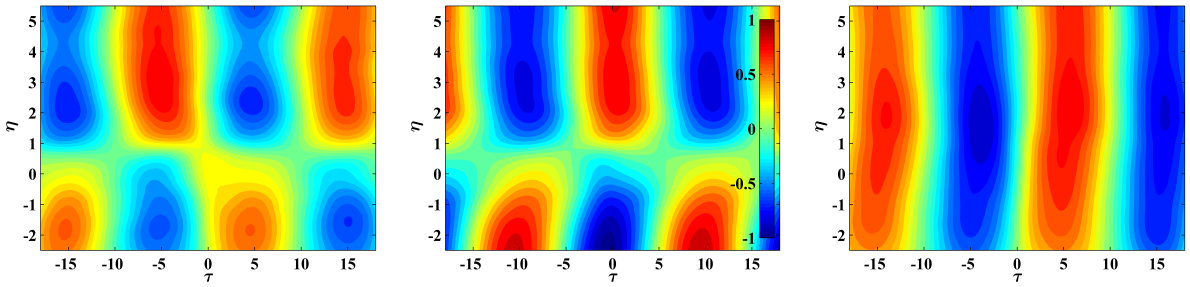

(a) $R_{u_x u_r}(x, \eta, \tau)$ (b) $R_{u_x p}(x, \eta, \tau)$ (c) $R_{u_r p}(x, \eta, \tau)$

Figure 14. Contours of velocity-pressure correlations at $x = 5$ from the ILES database for forcing with $m_F = 0$ and $St_{DF} = 0.3$. The common color-scale is shown in the middle figure.

IV.B. Predicting the model inflow pressure in experiments

The success of the vortex model documented above prompts the following modeling of the inflow pressure for the ROM of experimental data. Essentially, the velocity correlations in the experiments will be used to predict the pressure at the inflow boundary of the ROM by exploiting the velocity-pressure relation observed in the ILES database.

For experimental data, axial-to-radial velocity correlations with varying time-separations are not directly possible at present since time-resolved PIV is unfeasible at the flow time scales and domain sizes of interest. While this is strictly true for the unforced jet, an approximation may be made for the case of the forced jet. The forcing signal provides a readily identifiable phase relation in the data. The procedure for obtaining the correlations of interest is described next.

- Recall that the open-loop forcing experiments are performed at a fixed frequency and azimuthal mode. Stereo-PIV data is acquired on cross-stream slices (3 slices in as many separate runs) at $\sim$ 2 Hz, which makes the consecutive snapshots uncorrelated. However, the phase of actuation is also acquired simultaneous with the PIV snapshots.

- The sequence of snapshots are sorted in ascending order of their respective actuation phase. Next, the critical assumption is made that the structure organization due to forcing renders this sequence of snapshots into an approximation for a time-resolved velocity field.

- The above sequence is linearly interpolated onto a uniform phase space covering one forcing period. Three repetitions of the sequence are concatenated to exploit its periodicity in increasing the statistical significance of the ensuing correlation. This is the required approximation of the time-resolved three-component velocity field at a particular axial location, for all radial and azimuthal coordinates.

- It is assumed that the azimuthal Fourier mode of velocities corresponding to the forcing azimuthal mode are organized, so that this low-dimensional velocity field (at an arbitrary but fixed reference azimuthal angle) is extracted for each field.

- The final correlation step implements the formula presented earlier, with the omission of the integration over the azimuthal domain. The determination of the Fourier azimuthal mode of the velocity corresponding the forcing azimuthal mode has already incorporated this integration implicitly.

The open-loop experimental data for the forcing case of $m_F = 0$ and $St_{DF} = 0.3$ is investigated with the technique detailed above. The non-dimensionalized forcing period T_F is the reciprocal of St_{DF}. The results at three cross-stream slices in the axial domain of interest are presented in Figure 15. Comparison of Figure 15(a) with the corresponding results from the ILES database in Figure 14(a) reveals remarkable similarity in all aspects, including the strength and phase relations of correlations as well as the radial variation. This attests to the usefulness of forcing with LAFPA for educing time-resolved statistics in high-speed jets.

On further study of Figure 15, one notices very similar shapes of the correlation contours and phase relations, but a decrease of correlation levels in moving downstream. Also, there is a slight shift in the radial location of the changeover from lag to lead of the axial velocity fluctuations vis-a-vis the radial counterpart.

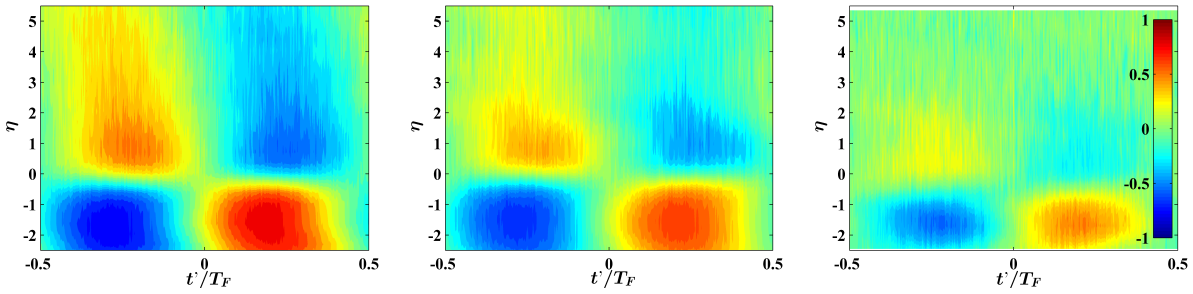

(a) $x = 5$ (b) $x = 6$ (c) $x = 7$

Figure 15. Contours of $R_{u_x u_r}(x, \eta, \tau)$ from experiments with forcing at $m_F = 0$ and $St_{DF} = 0.3$.

The potential core ends at $x \approx 6$ for this forcing case.[8] However, the core-like behavior is seen to persist up to $x = 7$ at the least. This has also been indicated by the phase-locked velocity fluctuations presented in Figures 13(d) and 13(e). The shift in the η of the changeover may be partially explained by the fact that the radial similarity variable does not account for the collapse of the potential core. However, the overall agreement of the velocity correlations obtained from the experimental and ILES databases with the vortex model of Lau et al. motivates the following modeling of the requisite pressure field.

The vortex model relates the approximate pressure, $\tilde{p}$, to the two-component velocity field at each point in the flow individually without assuming any spatial filtering:

$$\tilde{p}(x, r, \theta, t) = \frac{1}{T_1 + T_2} \int_{-T_1}^{T_2} L_x^*(\tau; x, r) u_x(x, r, \theta, t + \tau) \mathrm{d}\tau + \frac{1}{T_3 + T_4} \int_{-T_3}^{T_4} L_r^*(\tau; x, r) u_r(x, r, \theta, t + \tau) \mathrm{d}\tau. \quad (12)$$

This basically means that the pressure at any time t at a particular location is approximately determined by the behavior of the axial and radial velocities at that point over a window of time spanning t. The time constants T_1, T_2, T_3 and T_4 are left unspecified for now. The axisymmetry assumption removes the dependency of the model coefficients L_x and L_r on the azimuthal coordinate. It is expected that the model coefficients should vanish at large $|\tau|$. The asterisk refers to the complex conjugate, which is superfluous for the real quantities in the above expression, but are important in the following development.

The present objective is to predict the pressure in a forced jet. The following modifications are made to the above model for application to the problem at hand.

- The real-time velocity field information is required by the above model for predicting the pressure. This is not directly available. One could use the near-field pressure measurements to estimate this. However, such a strategy would make the control term somewhat self-referential. Instead, one needs to know the control term directly as a function of the actuation parameters, viz. frequency and phase. This means that the pressure approximated from the above model must be periodic, which in turn implies that one must extract the periodic part of the velocity field required by the model. This also means that the limits of time integration in eqn (12) may be set as $T_1 = T_2 = 0$ and $T_3 = T_4 = T_F$.

- The jet is forced at a particular azimuthal mode during any given run. It is assumed that the pressure field in the forced jet is also organized so that it can be fully represented by the same azimuthal mode. The linearity of the above model means that one needs to consider only the velocity field in the forced azimuthal mode. The azimuthal organization of the pressure field has been confirmed in experiments with schlieren imaging[37] as well as in numerical simulations.[2]

- The radial coordinate will be normalized as above so that the results from numerical simulations may be carried over to predict the pressure field in experiments.

The resulting model is

$$\tilde{\hat{p}}(x, \eta, t; m_F) = \frac{1}{T_F} \int_0^{T_F} L_x^*(\tau; x, \eta) \hat{u}_x(x, \eta, t + \tau; m_F) \mathrm{d}\tau + \frac{1}{T_F} \int_0^{T_F} L_r^*(\tau; x, \eta) \hat{u}_r(x, \eta, t + \tau; m_F) \mathrm{d}\tau. \quad (13)$$

Consider forcing of the jet using plasma actuators with time period T_F. The temporal direction is rendered approximately periodic by this forcing, so that any generic flow variable $w(t)$ may lend itself to

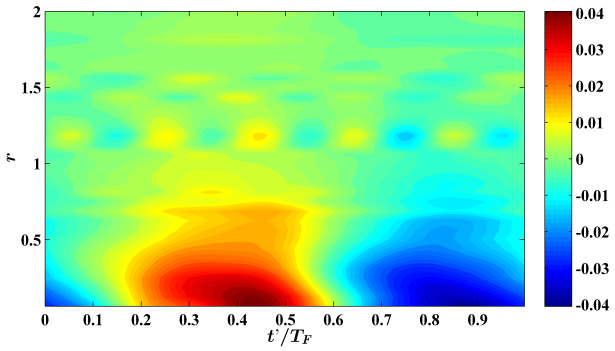

Figure 16. Estimated phase variation of axisymmetric mode of pressure fluctuations for forcing with $m_F = 0$ and $St_{DF} = 0.3$ at $x = 5$.

the temporal Fourier transform denoted by $w(t) \overset{\mathcal{F}_f}{\mapsto} \check{w}(k/T_F)$; $\check{w}(k/T_F) := (1/T_F)\int_0^{T_F} w(t)\mathrm{e}^{-2\pi \mathrm{i}kt/T_F}\mathrm{d}t$. Here k is the frequency mode. The inverse Fourier transform will be denoted by $\check{w}(k/T_F) \overset{\mathcal{F}_t}{\mapsto} w(t)$; $w(t) = \sum_{k=-\infty}^{\infty} \check{w}(k/T_F)\mathrm{e}^{2\pi \mathrm{i}kt/T_F}$.

To exploit the periodicity in the flow, one takes the temporal Fourier transform of the pressure prediction model in eqn (13) to obtain for any k

$$\check{\hat{p}}\left(x,\eta;m_F,\frac{k}{T_F}\right) = \check{L}_x^*\left(x,\eta,\frac{k}{T_F}\right)\check{\hat{u}}_x\left(x,\eta;m_F,\frac{k}{T_F}\right) + \check{L}_r^*\left(x,\eta,\frac{k}{T_F}\right)\check{\hat{u}}_r\left(x,\eta;m_F,\frac{k}{T_F}\right). \tag{14}$$

The pressure term required in the ROM is then recovered from the above estimate as

$$\hat{p}\,(x,r,t;m) \approx \delta_{m,m_F}\sum_{k=-K}^{K}\check{\hat{p}}\left(x,r;m_F,\frac{k}{T_F}\right)\mathrm{e}^{2\pi \mathrm{i}kt/T_F}, \tag{15}$$

where, K is the highest multiple of the fundamental forcing frequency retained through the temporal Fourier transform.

The above pressure approximation model is recognized as a straightforward spectral linear stochastic estimation problem.[38] The model coefficients are determined from the following set of linear equations involving the spectral correlations obtained from the ILES database

$$\begin{bmatrix}\check{L}_x(x,\eta,k/T_F)\\ \check{L}_r(x,\eta,k/T_F)\end{bmatrix} = \begin{bmatrix}S_{u_xu_x}(x,\eta,k/T_F) & S_{u_xu_r}(x,\eta,k/T_F)\\ S_{u_ru_x}(x,\eta,k/T_F) & S_{u_ru_r}(x,\eta,k/T_F)\end{bmatrix}^{-1}\begin{bmatrix}S_{u_xp}(x,\eta,k/T_F)\\ S_{u_rp}(x,\eta,k/T_F)\end{bmatrix}, \tag{16}$$

where, the spectral cross-correlations have the general definition

$$S_{\alpha\beta}(x,\eta,k/T_F) := \frac{1}{T_F}\int_0^{T_F}\Pi_{\alpha\beta}(x,\eta,t')\mathrm{e}^{-2\pi \mathrm{i}kt'/T_F}\mathrm{d}t', \tag{17}$$

where, the cross-correlation in the physical domain is defined in eqn (8).

The strategy for obtaining an approximation of the time-resolved velocity field from experiments in the forced jet has been outlined at the beginning of this sub-section. A temporal Fourier transform is performed on this approximate field to determine its frequency content. It is found that the first 4 temporal frequency modes capture almost all of the time variation. This velocity field is used in eqn (14) to approximate the pressure field. The result of this exercise is shown in Figure 16. The radial variation of the predicted pressure fluctuations is seen to agree with that found for the ILES database, as presented in Figure 13(c). The amplitudes observed in experiments are about a third of those seen in the ILES database, but this is to be expected from the corresponding differences in the respective velocity fields used for prediction.

With this approximate knowledge of the pressure variations over a forcing cycle, one can readily formulate a periodic form of the pressure term in eqn (6). Note that although this periodic variation is strictly valid for only a single forcing frequency and azimuthal mode, it could be extended to address the forcing parameters in a neighborhood in the parameter space.

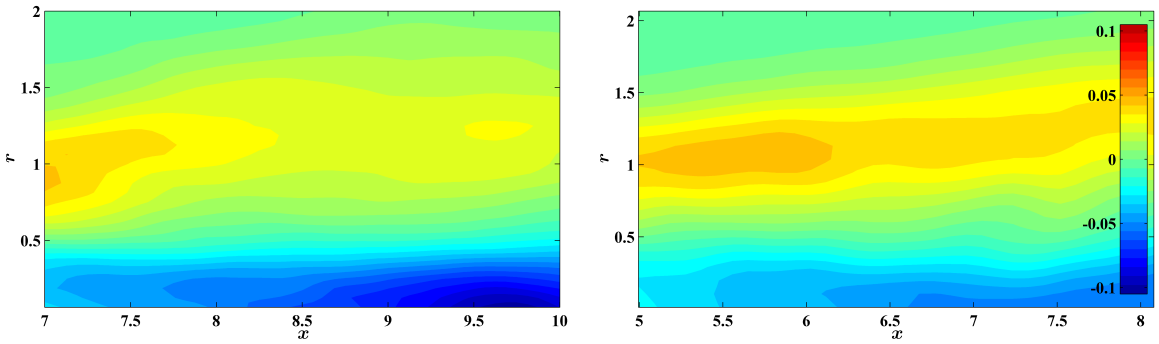

(a) Simulation of ROM from DNS

(b) Experimental data

Figure 17. Contours of the difference in mean axial velocity field of the forced case over the unforced. The forcing case is $m_F = 0$ and $St_{DF} = 0.3$. The color-scale is the same for both plots.

IV.C. Validating the actuator model

The validation of the periodic actuation model necessitates a ROM whose trajectories remain bounded for a long time. As discussed previously, the ROMs derived from the experimental and ILES databases did not satisfy this requirement. On the other hand, a 44-dimensional ROM from the DNS database did have bounded trajectories for over 5000 flow time scales, and thus was used in the present validation effort.

It has been discussed in Ref. 10 that owing to the initial boundary layer being laminar for the DNS jet, its potential core is longer than in the experimental jet. In fact, the modeling domain for the DNS database extends from $x = 7$ to 10 to capture similar dynamics as observed in the domain from $x = 5$ to 8 in both experimental and ILES databases. Thus, for the actuation term in the ROM of the DNS, one is looking for the periodic pressure field at $x = 7$, the field at $x = 10$ being much weaker per previous arguments.

The DNS database consists of a single case, namely the unforced jet. So, the technique for educing the periodic pressure field at the inflow boundary developed above for experimental data is not applicable. However, one can use the periodic pressure field at $x = 5$ from the ILES database directly. This involves several approximations. However, it is arguable that this is justified for the purpose of validation of the concept behind the modeling of LAFPA actuation.

The ROM derived from the DNS database was simulated without and with actuation at $m_F = 0$ and $St_{DF} = 0.3$ for 5000 flow time steps. Figure 17(a) shows the change in the mean axial velocity field with actuation, compared to the mean field computed from the original DNS database. This is to be compared with Figure 17(b) wherein a similar differential mean field is shown from streamwise 2C-PIV data obtained in the respective forcing cases in experiments. The similarity of the two contour plots in both shape and magnitude is striking, given the numerous modeling assumptions discussed above. Both show the increased mixing obtained with this forcing, resulting in a smaller potential core and a flared shear layer.

The simulated database was then sampled at a fixed phase on each forcing period to mimic a phase-locked PIV experiment. Since this is an axisymmetric forcing case, an azimuthal averaging is performed in addition to the phase-averaging. Subtraction of the simulated mean field gives the phase-averaged fluctuations. Figure 18(a) shows the axial component of the phase-averaged fluctuations from the simulation of the ROM obtained from the DNS database. This is to be compared with Figure 18(b) which is a zoomed and re-scaled version of Figure 3(b). Overall shape and wavelength in the two cases are again strikingly similar. However, the simulations have about half the amplitude of fluctuations observed in experiments.

Another way of looking at the effect of forcing is to study the power spectral density (PSD) of velocity fluctuations at a salient point in the flow. Since the forcing is axisymmetric, the PSDs computed over an azimuthal circle were averaged to obtain a smoother spectrum. For the simulated DNS field, the chosen location was $x = 8.2$ and $r = 0.5$. Figure 19(a) first compares the PSD computed from the simulation of the unforced jet to that computed from the original DNS database. The low-frequency behavior is captured very well by the simulation, although the high-frequency end shows the rapid roll-off expected from the severe truncation of the POD and azimuthal bases. The PSD computed from the simulation of the forced jet is also presented. Apart from a forcing tone, this does not show much departure from the simulation of the unforced jet. To assess whether this behavior is indeed to be expected, a comparison is desired. Unfortunately, there is no time-resolved experimental data at hand for assessing this. Instead, we resort to the ILES database,

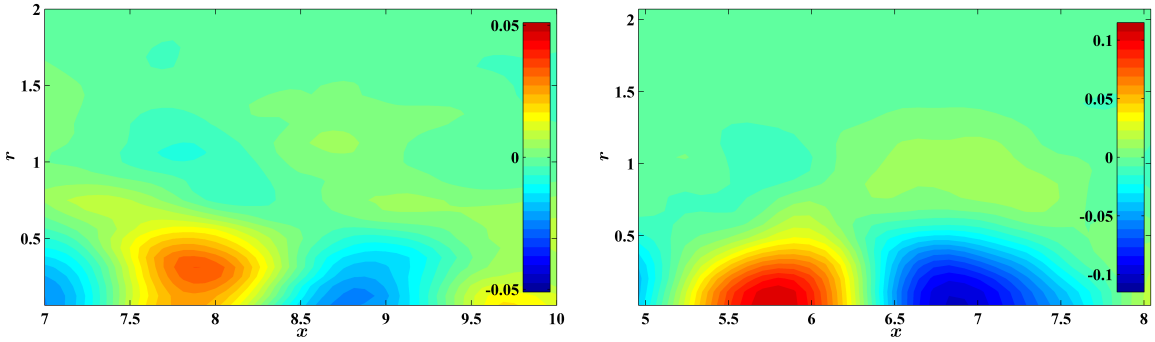

(a) Simulation of ROM from DNS (b) Experimental data

Figure 18. Contours of the phase-averaged fluctuations in the axial velocity with forcing at $m_F = 0$ and $St_{DF} = 0.3$.

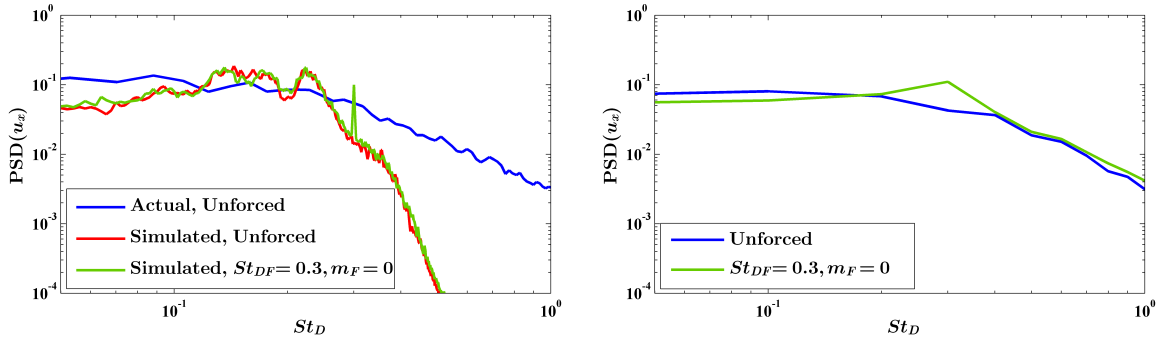

(a) Simulation of ROM for DNS at $x = 8.2$, $r = 0.5$ (b) ILES data at $x = 6$, $r = 0.5$

Figure 19. Power spectral density of axial velocity field at salient points in the flow domain. In all cases with forcing, m_F was 0 and St_{DF} was 0.3.

and the computed PSD at an equivalent location is shown in Figure 19(b). Note that the total length of time over which we have this data is 20 flow time scales; thus the frequency axis of this PSD is poorly resolved. However, the change of the PSD with forcing is very similar to that observed in simulations. As an aside, note that the PSD for the unforced ILES jet is very similar to that of the unforced DNS jet, even with the large difference in Reynolds number and Mach number. This provides some justification for the use of the pressure field from the ILES database to formulate the forcing term for the ROM of the DNS jet.

V. Conclusion

The attenuation of jet noise and the enhancement of jet bulk mixing using localized arc filament plasma actuators are posed as feedback control problems. Extensive experiments detailed herein has been performed to obtain an empirical database suited to the development of a reduced-order model for this purpose. The database includes both unforced and salient forced cases. Three main results are reported in this article. First, a low-dimensional description of the kinematics of the forced jet data can be obtained using the low-dimensional functional basis educed from the kinematics of the unforced jet. Second, the reduced-order modeling procedure for the jet dynamics developed previously is validated using the data from the unforced case. Third, a technique is proposed for modeling the actuation effects and it is successfully applied for replicating the behavior of the forced jet.

Acknowledgments

The research is supported in part by the Air Force Office of Scientific Research with Dr. John Schmisseur as the program manager, NASA Glenn Research Center with Drs. James Bridges and Cliff Brown, and by a fellowship from the Ohio State University to the first author. We would like to thank Drs. Jonathan Freund

and Datta Gaitonde for the permission to use their simulation databases. Finally, gracious acknowledgement is due to our colleagues in GDTL - Michael Crawley, Martin Kearney-Fischer, and Casey Hahn - for extensive guidance and assistance with the experiments.

References

[1]Freund, J. B., "Noise sources in a low-Reynolds-number turbulent jet at Mach 0.9," *Journal of Fluid Mechanics*, Vol. 438, No. 1, 2001, pp. 277–305.

[2]Gaitonde, D. V., "Simulation-based analysis of the near field in a supersonic jet controlled by plasma actuators," *49th AIAA Aerospace Sciences Meeting, AIAA Paper 2011-23*, 2011.

[3]Gutmark, E. J., Schadow, K. C., and Yu, K. H., "Mixing Enhancement in Supersonic Free Shear Flows," *Annual Review of Fluid Mechanics*, Vol. 27, No. 1, 1995, pp. 375–417.

[4]Jordan, P. and Gervais, Y., "Subsonic jet aeroacoustics: associating experiment, modelling and simulation," *Experiments in Fluids*, Vol. 44, No. 1, 2008, pp. 1–21.

[5]Samimy, M., Kim, J.-H., Kastner, J., Adamovich, I., and Utkin, Y., "Active control of high-speed and high-Reynolds-number jets using plasma actuators," *Journal of Fluid Mechanics*, Vol. 578, 2007, pp. 305–330.

[6]Samimy, M., Kim, J.-H., Kastner, J., Adamovich, I., and Utkin, Y., "Active control of a Mach 0.9 jet for noise mitigation using plasma actuators," *AIAA Journal*, Vol. 45, No. 4, 2007, pp. 890–901.

[7]Utkin, Y. G., Keshav, S., Kim, J.-H., Kastner, J., Adamovich, I. V., and Samimy, M., "Development and use of localized arc filament plasma actuators for high-speed flow control," *Journal of Physics D: Applied Physics*, Vol. 40, No. 3, 2007, pp. 685–694.

[8]Kearney-Fischer, M., Kim, J.-H., and Samimy, M., "Control of a High Reynolds Number Mach 0.9 Heated Jet Using Plasma Actuators," *Physics of Fluids*, Vol. 21, 2009, pp. 095101.

[9]Samimy, M., Kim, J.-H., Kearney-Fischer, M., and Sinha, A., "Acoustic and flow fields of an excited high Reynolds number axisymmetric supersonic jet," *Journal of Fluid Mechanics*, Vol. 656, 2010, pp. 507–529.

[10]Sinha, A., Serrani, A., and Samimy, M., "Initial development of reduced-order models for feedback Control of axisymmetric jets," *International Journal of Flow Control*, Vol. 2, No. 1, 2010, pp. 39–60.

[11]Holmes, P., Lumley, J., and Berkooz, G., *Turbulence, Coherent Structures, Dynamical Systems and Symmetry*, Cambridge University Press, 1996.

[12]Gaitonde, D. V. and Samimy, M., "Effect of plasma-based azimuthal mode excitation on supersonic jet flow," *5th AIAA Flow Control Conference, AIAA Paper 2010-4416*, 2010.

[13]Lumley, J. L., "The Structure of Inhomogeneous Turbulent Flows," *Atm. Turb. and Radio Wave Prop.*, edited by A. M. Yaglom and V. I. Tatarsky, Nauka, Moscow, 1967, pp. 166–178.

[14]Sirovich, L., "Turbulence and the dynamics of coherent structures, Parts I-III," *Quarterly of Applied Mathematics*, Vol. XLV, No. 3, 1987, pp. 561–590.

[15]Tinney, C. E., Glauser, M. N., and Ukeiley, L. S., "Low-dimensional characteristics of a transonic jet. Part 1. Proper orthogonal decomposition," *Journal of Fluid Mechanics*, Vol. 612, 2008, pp. 107–141.

[16]Tinney, C. E., Ukeiley, L. S., and Glauser, M. N., "Low-dimensional characteristics of a transonic jet. Part 2. Estimate and far-field prediction," *Journal of Fluid Mechanics*, Vol. 615, 2008, pp. 53–92.

[17]Samimy, M., Adamovich, I., Webb, B., Kastner, J., Hileman, J., Keshav, S., and Palm, P., "Development and characterization of plasma actuators for high-speed jet control," *Experiments in Fluids*, Vol. 37, No. 4, 2004, pp. 577–588.

[18]Konstantinidis, E., Balabani, S., and Yianneskis, M., "Conditional averaging of PIV plane wake data using a cross-correlation approach," *Experiments in Fluids*, Vol. 39, 2005, pp. 38–47.

[19]Boree, J., "Extended Proper Orthogonal Decomposition: A Tool to Analyse Correlated Events in Turbulent Flows," *Experiments in Fluids*, Vol. 35, No. 2, 2003, pp. 188–192.

[20]Fogleman, M., Lumley, J., Rempfer, D., and Haworth, D., "Application of the proper orthogonal decomposition to datasets of internal combustion engine flows," *Journal of Turbulence*, Vol. 5, No. 23, 2004, pp. 1–18.

[21]Taylor, J. A. and Glauser, M. N., "Towards Practical Flow Sensing and Control via POD and LSE Based Low-Dimensional Tools," *ASME Journal of Fluids Enginnering*, Vol. 126, No. 3, 2004, pp. 337–345.

[22]Pinier, J. T., Ausseur, J. M., Glauser, M. N., and Higuchi, H., "Proportional Closed-Loop Feedback Control of Flow Separation," *AIAA Journal*, Vol. 45, No. 1, 2007, pp. 181–190.

[23]Caraballo, E., Kasnakoğlu, C., Serrani, A., and Samimy, M., "Control Input Separation Methods for Reduced-Order Model-Based Feedback Flow Control," *AIAA Journal*, Vol. 46, No. 9, 2008, pp. 2306–2322.

[24]Zheng, X. and Glauser, M. N., "A low dimensional description of the axisymmetric jet mixing layer," *ASME Computers in Engineering*, Vol. 2, 1990, pp. 121–127.

[25]Jung, D. H., Gamard, S., and George, W. K., "Downstream evolution of the most energetic modes in a turbulent axisymmetric jet at high Reynolds number. Part 1. The near-field region," *Journal of Fluid Mechanics*, Vol. 514, 2004, pp. 173–204.

[26]Iqbal, M. O. and Thomas, F. O., "Coherent structure in a turbulent jet via a vector implementation of the proper orthogonal decomposition," *Journal of Fluid Mechanics*, Vol. 571, 2007, pp. 281–326.

[27]Kim, J.-H., Kastner, J., and Samimy, M., "Active Control of a High Reynolds Number Mach 0.9 Axisymmetric Jet," *AIAA Journal*, Vol. 47, No. 1, 2009, pp. 116–128.

[28]Kastner, J., Kim, J.-H., and Samimy, M., "A study of the correlation of large-scale structure dynamics and far-field radiated noise in an excited Mach 0.9 jet," *International Journal of Aeroacoustics*, Vol. 8, No. 3, 2009, pp. 231–259.

[29]George, W. K., Beuther, P. D., and Arndt, R. E. A., "Pressure spectra in turbulent free shear flows," *Journal of Fluid Mechanics*, Vol. 148, No. 1, 1984, pp. 155–191.

[30]Rajaee, M., Karlsson, S. K. F., and Sirovich, L., "Low-dimensional description of free-shear-flow coherent structures and their dynamical behaviour," *Journal of Fluid Mechanics*, Vol. 258, 1994, pp. 1–29.

[31]Rempfer, D. and Fasel, H. F., "Dynamics of three-dimensional coherent structures in a flat-plate boundary layer," *Journal of Fluid Mechanics*, Vol. 275, 1994, pp. 257–283.

[32]Cazemier, W., Verstappen, R. W. C. P., and Veldman, A. E. P., "Proper orthogonal decomposition and low-dimensional models for driven cavity flows," *Physics of Fluids*, Vol. 10, No. 7, 1998, pp. 1685–1699.

[33]Lau, J. C., Fisher, M. J., and Fuchs, H. V., "The Intrinsic Structure of Turbulent Jets," *Journal of Sound and Vibration*, Vol. 22, No. 4, 1972, pp. 379–406.

[34]Lau, J. C. and Fisher, M. J., "The vortex-street structure of 'turbulent' jets. Part 1," *Journal of Fluid Mechanics*, Vol. 67, No. 2, 1975, pp. 299–337.

[35]Bodony, D. J. and Lele, S. K., "On using large-eddy simulation for the prediction of noise from cold and heated turbulent jets," *Physics of Fluids*, Vol. 17, 2005, pp. 085103.

[36]Fleury, V., Bailly, C., Jondeau, E., Michard, M., and Juve, D., "SpaceTime Correlations in Two Subsonic Jets Using Dual Particle Image Velocimetry Measurements," *AIAA Journal*, Vol. 46, No. 10, 2008, pp. 2498–2509.

[37]Hahn, C., Kearney-Fischer, M., and Samimy, M., "Effects of ring groove and duty cycle on plasma actuator performance in high speed jets," *49th AIAA Aerospace Sciences Meeting, AIAA Paper 2011-977*, 2011.

[38]Tinney, C. E., Coiffet, F., Delville, J., Hall, A. M., Jordan, P., and Glauser, M. N., "On spectral linear stochastic estimation," *Experiments in Fluids*, Vol. 41, No. 5, 2006, pp. 763–775.